A Lagrangian analysis of cold cloud clusters and their life cycles with satellite observations

Rebekah Bradley Esmaili[1], Yudong Tian[2], Daniel Alejandro Vila[3], and Kyu-Myong Kim[4]

[1]Department of Atmospheric and Oceanic Science, University of Maryland, College Park, Maryland, USA, [2]Earth System Science Interdisciplinary Center, University of Maryland, College Park, Maryland, USA, [3]National Institute for Space Research (INPE), São José dos Campos, Brazil, [4]NASA Goddard Space Flight Center, Greenbelt, Maryland, USA

Abstract Cloud movement and evolution signify the complex water and energy transport in the atmosphere-ocean-land system. Detecting, clustering, and tracking clouds as semicoherent clusters enable study of their evolution which can complement climate model simulations and enhance satellite retrieval algorithms, where there are gaps between overpasses. Using a cluster tracking algorithm, in this study we examine the trajectories, size, and brightness temperature of millions of cloud clusters over their lifespan, from infrared satellite observations at 30 min, 4 km resolution, for a period of 11 years. We found that the majority of cold clouds were both small and short lived and that their frequency and location are influenced by El Niño. Also, this large sample of individually tracked clouds shows their horizontal size and temperature evolution. Long-lived clusters tended to achieve their temperature and size maturity milestones at different times, while these stages often occurred simultaneously in short-lived clusters. On average, clusters with this lag also exhibited a greater rainfall contribution than those where minimum temperature and maximum size stages occurred simultaneously. Furthermore, by examining the diurnal cycle of cluster development over Africa and the Indian subcontinent, we observed differences in the local timing of the maximum occurrence at different life cycle stages. Over land there was a strong diurnal peak in the afternoon, while over the ocean there was a semidiurnal peak composed of longer-lived clusters in the early morning hours and shorter-lived clusters in the afternoon. Building on regional specific work, this study provides a global long-term survey of object-based cloud characteristics.

1. Introduction

Clouds are the most visible vital sign of the atmosphere's dynamic water and energy transfer. They are responsible for the latent heat release that drives the atmospheric circulation. Their transport of water in the form of moisture and precipitation is critical for the Earth's hydrological cycle. On subsynoptic scales, the cloud systems' movement, evolution, and spatial and temporal characteristics are remarkably turbulent and complex.

The Lagrangian framework is an effective approach to study cloud clusters. Treating each cloud as an object across its lifespan produces useful information on the evolution of cloud systems' properties, which is not available from the Eulerian view [*Machado et al.*, 1998]. Renewed interest in cloud object-based evolution is partly due to the advancement of satellite-based multisensor high-resolution precipitation estimates [*Li et al.*, 2015]. Currently, these estimates rely heavily on observations from passive microwave (PMW) sensors aboard polar-orbiting satellites [*Kummerow et al.*, 2000; *Joyce et al.*, 2004; *Huffman et al.*, 2007, 2013]. These PMW-based estimates are relatively accurate, but they do not correlate well with surface observations when precipitation is very light, very heavy, or over saturated land surfaces, particularly during winter months [*Ebert et al.*, 2007]. Additionally, these data have large spatial and temporal gaps.

One way to bridge these coverage gaps is to use cloud system advection information derived from high-resolution infrared observations to continuously "morph" the PMW-based rainfall [*Joyce et al.*, 2004; *Kubota and Shige*, 2007; *Xie and Xiong*, 2011]. These approaches have been proven effective and are being incorporated into Integrated Multi-satellitE Retrievals for GPM (IMERG) [*Huffman et al.*, 2013], the next-generation, Global Precipitation Measurement (GPM) [*Hou et al.*, 2013] era product suite. However, the accuracy of the PMW-based estimates is also influenced by the life cycle stage [*Tadesse and Anagnostou*, 2009]. Developing a more detailed understanding of evolution can provide additional context.

Another critical application is the evaluation and diagnosis of global models. Currently, atmospheric models still unrealistically reproduce observed precipitation [*Ebert et al.*, 2007; *Stephens et al.*, 2010]. The conventional

Eulerian validation gives the spatial and temporal statistics on each individual grid box, which is the accumulation of many different cloud systems at various life stages. A Lagrangian comparison of modeled and observed cloud evolution statistics could produce additional insight on the modeling of individual cloud-precipitation processes [*Boer and Ramanathan*, 1997].

In the past, studies that combined infrared satellite-based cloud cluster tracking with Tropical Ocean–Global Atmosphere field campaign to examine cloud evolution, anatomy, and development conditions [*Williams and Houze*, 1987; *Chen and Houze*, 1997]. On larger scales, mesoscale convective systems (MCS) have in particular been studied due to their ease of detection in radar and satellite images and destructiveness [*Maddox*, 1980; *Laing and Fritsch*, 1997; *Blamey and Reason*, 2012]. MCS display regularity in their life cycles, enabling *Machado and Laurent* [2004] to develop a statistical life cycle model to predict MCS propagation with good forecasting skill.

As global, long-term, quality controlled IR data and precipitation data become available [e.g., *Janowiak et al.*, 2001; *Joyce et al.*, 2004], it becomes feasible to extend IR-based cloud tracking beyond regional scales and expand the scales of observed phenomena. By following a large number of cloud clusters on the global scale for over 11 years, we will be able to understand more systematically their large-scale dynamical and statistic characteristics.

In this paper, we present a near-global (60°S–60°N), high-resolution (30 min, 4 km), long-term (11 year) study of cloud cluster tracks, life cycle evolution, and diurnal cycle. The high-resolution data used for the study and the methodology for storm tracking are described in sections 2 and 3, respectively. Section 4 presents the results followed by summary and discussions in section 5.

2. Data

For our study, we use the National Centers for Environmental Prediction/Climate Prediction Center (NCEP/CPC) a 4 km, half-hourly infrared (IR) brightness temperature data set [*Janowiak et al.*, 2001]. The data set is merged from all available geostationary satellites (GMS, Meteosat-5, Meteosat-7, GOES 8, and GOES 10) to form near-global (60°N–60°S) coverage on a uniform latitude-longitude grid. We used 11 years of data from 2002 to 2012 for our study.

We have performed additional quality control of the IR data. There are gaps in the IR data in regions covered by the GMS satellite in the western Pacific (120°–170°E), so we filled the missing data by interpolating the preceding and following 30 min snapshots, to produce more seamless coverage. Our tests show that this interpolation helps to prevent early termination of the cloud lifespan due to missing data.

3. Methodology

The techniques for tracking clouds are mature and largely similar, albeit there are many implementations. Most of those techniques involve IR geostationary satellite imagery to follow classes of convective events. The primary dissimilarities in algorithms involve the detection criteria, such as through the selection of brightness temperature or size parameter thresholds [*Carvalho and Jones*, 2001; *Morel and Senesi*, 2002], usage of more nuanced detection schemes [*Lakshmanan et al.*, 2009], or the treatment of splits and merges [*Fiolleau and Roca*, 2013].

In spite of a variety of implementations, *Machado et al.* [1998] found that most of the life cycle statistics are not overly sensitive to the tracking method used. For this paper, we selected Forecast and Tracking the Evolution of Cloud Clusters (ForTrACC) [*Vila et al.*, 2008] which has a single temperature and system size threshold and merges and splits are treated as special cases for tracking systems (this will be explained in section 3.2). ForTrACC's simplicity enabled us to capture a broader range of cloud species.

Tracking clouds involves the following two major steps.

3.1. Identification Using Temperature and Morphology

Using brightness temperature thresholds to capture clouds has been used in past studies and typically empirically derived to satisfy the research goals [e.g., *Blamey and Reason*, 2012; *Velasco and Fritsch*, 1987; *Williams and Houze*, 1987]. In general, brightness temperature detection thresholds vary between 235 and 255 K and tended to be subjectively chosen. However, the cluster areal extent was found to the linearly
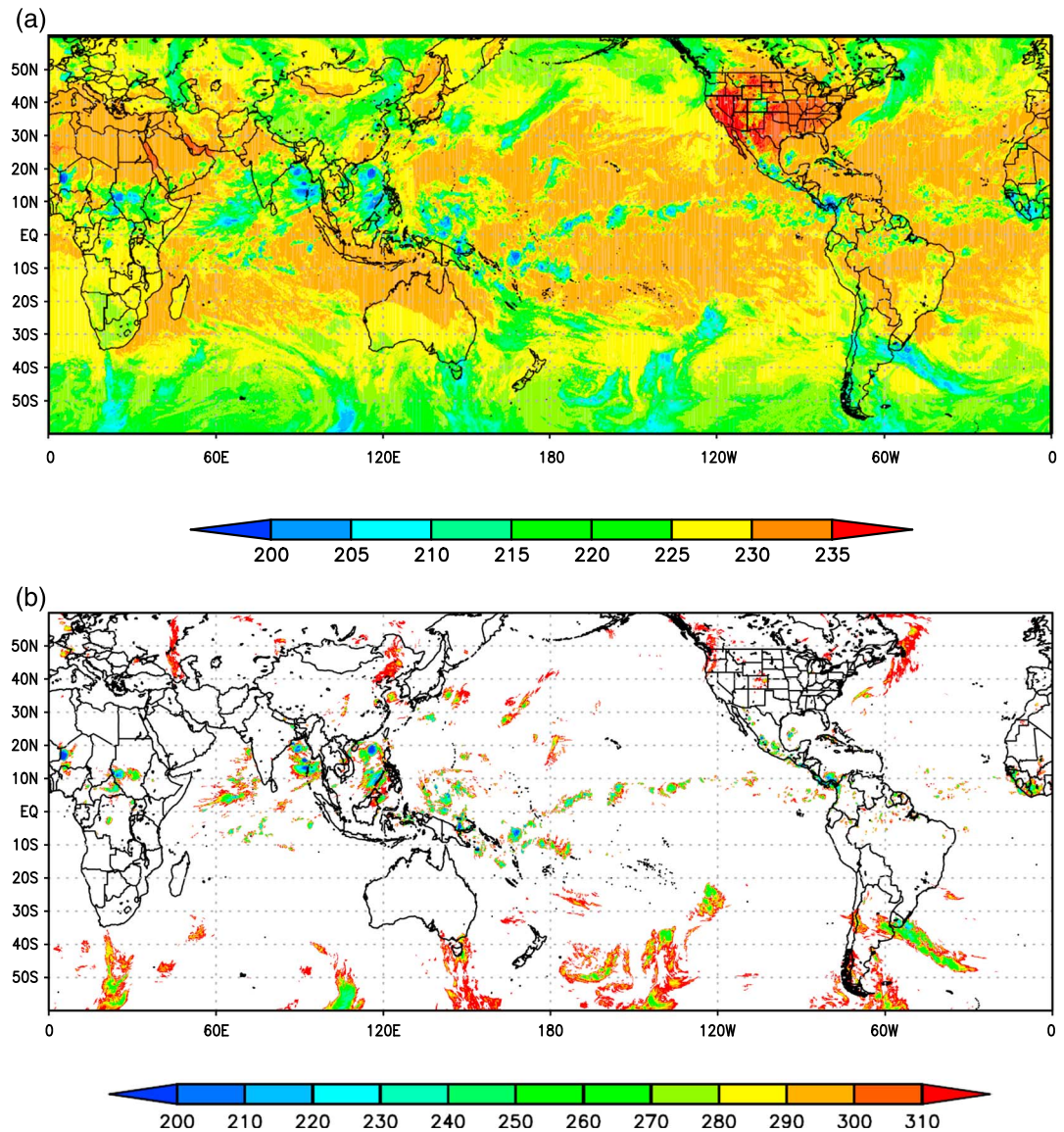
Figure 1. (a) Globally merged map of IR brightness temperature from NCEP/CPC Cloud brightness temperature data set for 23:00 greenwich mean time 28 June 2012. (b) Cloud clusters captured by ForTraCC after applying temperature and size thresholds. Shading represents cloud brightness temperature.

dependent on cluster threshold and thus not overly sensitive to the exact threshold chosen [*Machado et al.*, 1992; *Mapes and Houze*, 1993].

To capture a variety of cloud clusters, we used a single 235 K brightness temperature threshold, which in the upper atmosphere corresponds to a height of roughly 10 km (9 km) in the tropics (midlatitudes), which is well into the free atmosphere. Additionally, we applied a minimum size threshold of 100 contiguous pixels (1600 km^2 at the equator) at all time steps, thus limiting the study to events at the upper bounds of mesoscale or larger. We excluded smaller-scale events because they would be more suitable for regional studies. Figure 1 shows this selection criteria being applied to a typical IR snapshot. A temperature range of 235–245 K has been used in the past to detect cloud clusters [e.g., *Williams and Houze*, 1987; *Mapes and Houze*, 1993; *Carvalho and Jones*, 2001; *Machado and Laurent*, 2004]; the colder threshold is utilized to avoid capturing frozen, high-altitude surfaces. The size threshold reduces the number of tracked clouds by filtering out small-scale events and reducing the number of splits and merges. With only a temperature threshold, a single time step can yield over 17,000 cloud clusters. Applying the size threshold decreased to the number to 800–1000 events.
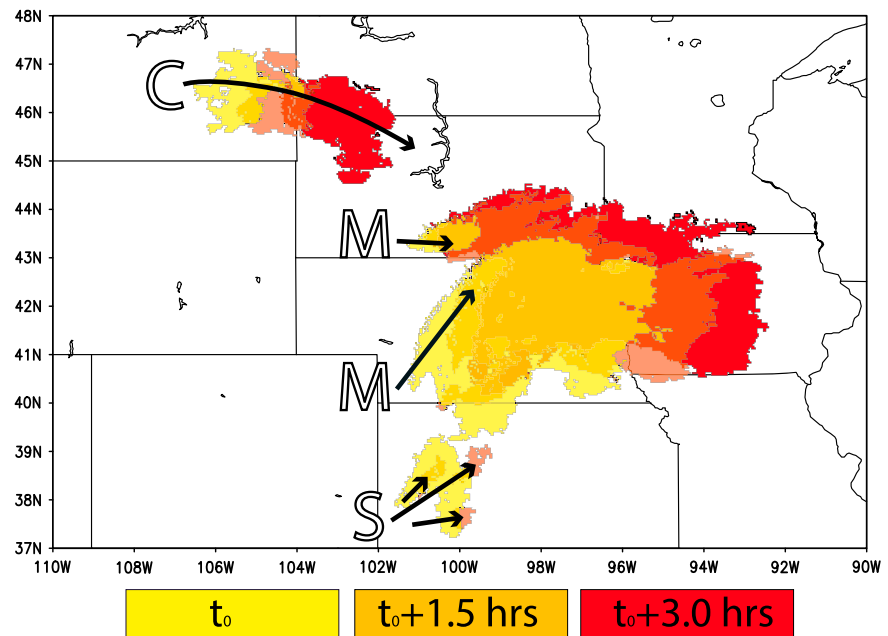
Figure 2. Schematic of area overlap handling of continuous systems (c), merging systems (m), and splitting systems (s). The image was taken of thunderstorms developing over the American Midwest beginning at 3:00 pm EST on 30 June 2012. Yellow represents the initial time, orange 1.5 h later, and red 3.0 h after initial detection.

3.2. Tracking Using Area Overlap

ForTrACC uses an area overlap technique to track the cloud clusters, both forward and backward in time. If two cloud clusters identified in different time steps have any shared pixels, they were considered the same system and assigned a family number. If more than one match was found, the largest overlaping system was tracked.

Using infrared data, we show in Figure 2 a schematic of the area overlap handling in ForTrACC. The area overlap technique produces several cloud cluster merge scenarios: one-to-one (continuous), one-to-many (split), many-to-one (merge), or no match (initialization or dissipation). Most systems undergo merging or splitting in their life cycle, the prior occurs before maturation, and the latter more frequently toward the end of the life cycle. Only one cluster is followed at each time step to keep features well defined. When clusters split, the largest cloud continues to be tracked, while the smaller-split clusters are treated as a new family and the lifetime clock is reset. All merging clusters are considered a dissipation, and their life cycle ends. ForTrACC's handling of split and merge segments is different from earlier work; in other schemes, the segments remain part of the cloud cluster system rather than considered new systems [*Mapes and Houze*, 1993; *Chen et al.*, 1996; *Chen and Houze*, 1997].

A sample output of the resulting cloud cluster tracks is shown in Figure 3. In addition to showing centroid location, statistics related to the size or areal extent, the mean brightness temperature, and travel distance of the cluster are also calculated. Colder temperatures indicate higher-cloud tops, while areal extent shows the relative scale of the observed system. All clusters achieve a minimum temperature and maximum size, which we use as criteria for developmental maturity in section 4.5. We use this information to study the ForTrACC-based cloud clusters' statistical properties, climatology, life cycle, rainfall contribution, and diurnal cycle.

3.3. Collocation of Clusters With Passive Microwave Rainfall Estimations

To examine the rainfall contribution of cloud clusters, we matched PMW precipitation estimates from IMERG [*Huffman et al.*, 2013] with spatially and temporally collocated cloud clusters.

While Tropical Rainfall Measuring Mission (TRMM)-based products have a longer data record, GPM has global coverage so we selected 2 months of data to examine (June and December 2014). Both data sets were scaled to a common grid ($0.1° \times 0.1°$), and the available rainfall totals were summed for clusters at various life cycle stages.
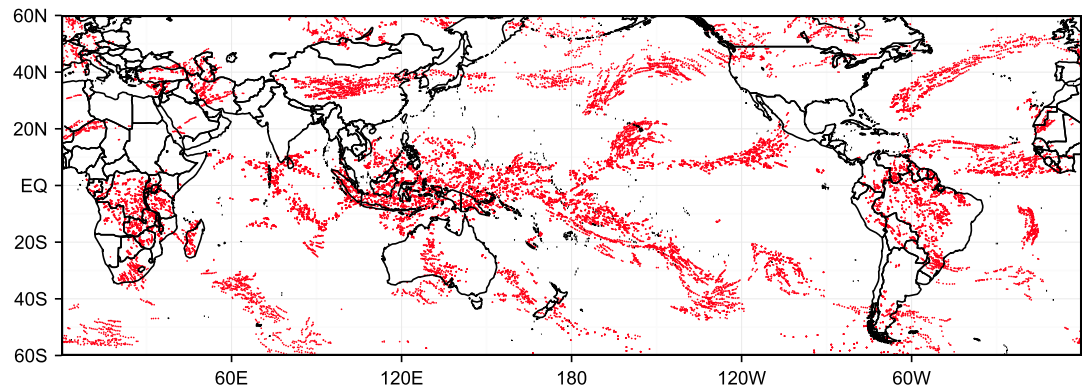
Figure 3. Cloud cluster tracks from 1–4 December 2001 produced from using the ForTrACC algorithm. A few days of tracking yield a large number of clusters, and their movement begins to trace out large-scale atmospheric patterns.

4. Results

4.1. Mean Trajectories and Statistical Properties of Cloud Clusters

Tracking on the global scale builds on regional studies and enables us to document many fundamental statistical characteristics of cloud clusters. At any instant, there are on average 800 clusters larger than 1600 km^2 in the Earth's atmosphere between 60°S and 60°N. Figure 4 shows the global distribution of clusters with lifetimes between 6 and 9 h, for both December through February (DJF) and June through August (JJA). The
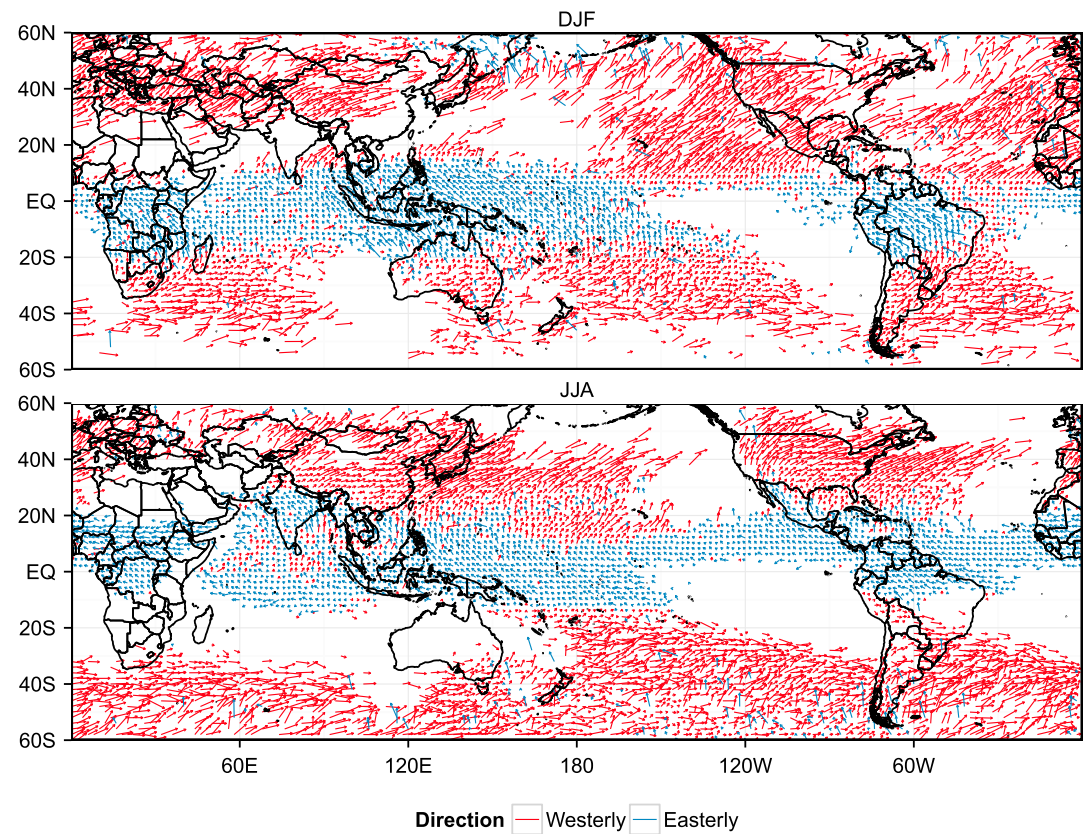

Figure 4. Climatology of cloud cluster trajectories in (top) DJF and (bottom) JJA, 2002–2012 with 6–9 h lifetimes binned by 2° × 2°. Lines show average displacement of all cloud clusters that initiated at the same point over the 11 year period studied. Coloring indicates net zonal movement of clusters. Grid boxes with fewer than five initiations were not displayed.
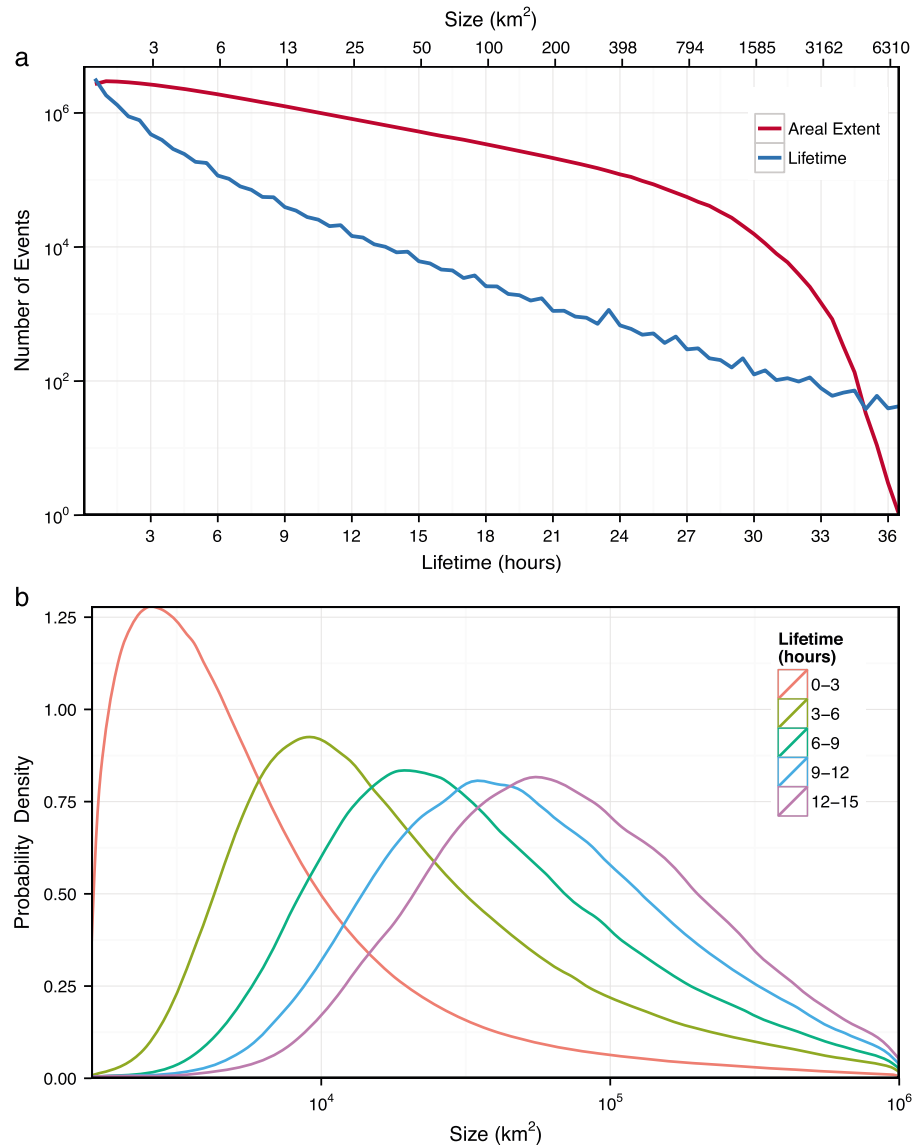
Figure 5. (a) Number of detected events globally by lifetime and size for the entire record. (b) The kernel density estimate of cloud clusters at their maximum areal extent for each lifetime group over the entire study period (DJF and JJA, 2002–2012).

mean trajectories are calculated by averaging the endpoints of all cluster centroids that initiate at the same 2° × 2° binned latitude and longitude coordinates. The colors represent the net zonal direction of the flow.

Regarding the zonal average distance traveled by 6–9 h lifetime clusters in Figure 4, we found that cloud clusters travel farther in the Northern Hemisphere during DJF; the average distance traveled peaks at 644.8 km at 36°N, which is likely due to influence of the climatological jet stream on development and propagation. In the Southern Hemisphere the maximum occurs near 52°S at a lower 419.8 km. Movement in the tropics does not vary drastically from each season, but the peak (189.1 km) occurs in JJA at 12°N. This is in part due to the persistence of the Intertropical Convergence Zone (ITCZ) and African Easterly Wave activity.

Cloud clusters can last from a few hours up to 2 days, and their sizes range from our minimal threshold to more than 10^6 km^2 (Figure 5). Most of the clusters are short lived and small (Figure 5a), with 90% of the clusters detected having a size less than 49,275 km^2 and a lifetime less than 5 h. The cluster lifetime distribution follows roughly a log linear distribution, while the cluster size distribution appears to be lognormal at certain scales, the latter being consistent with some past findings [*Machado et al.*, 1992; *Mapes and Houze*, 1993] but
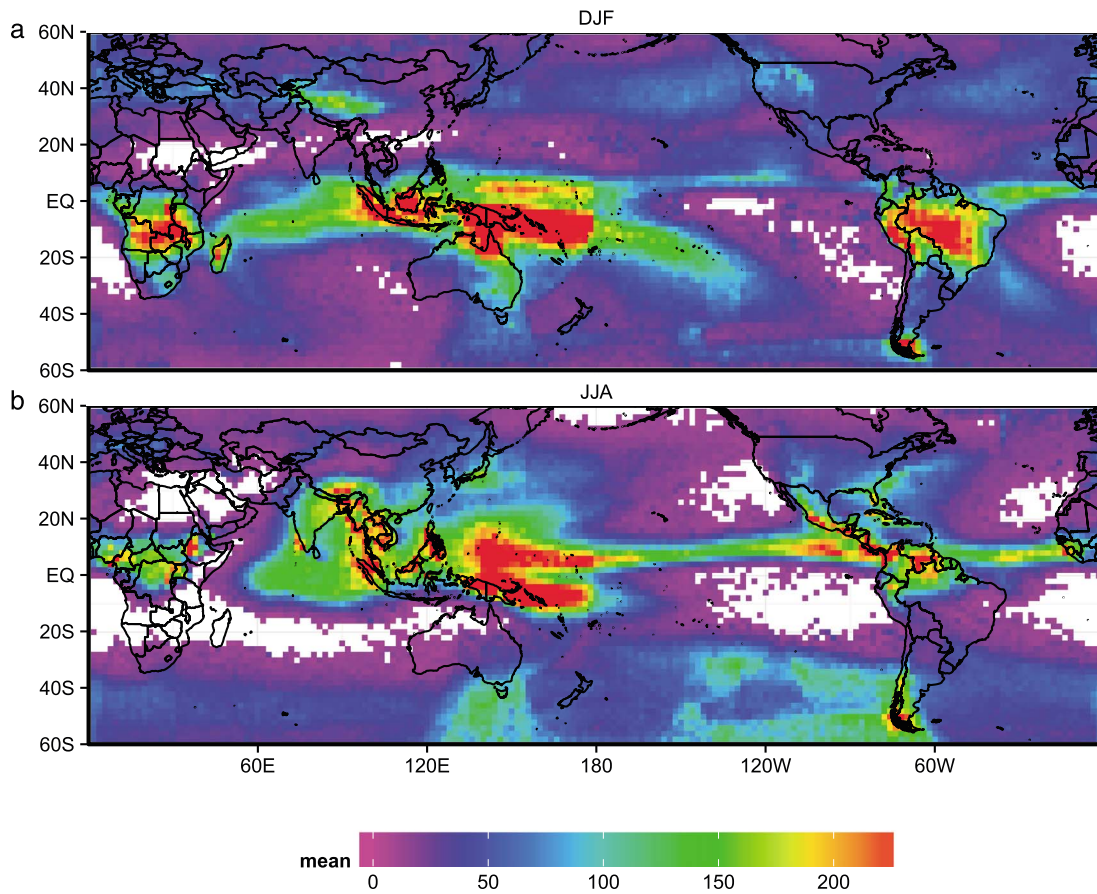
Figure 6. Mean seasonal frequency of clusters for (a) DJF and (b) JJA at their maximum areal extent. The figure shows the average seasonal count of events over the study period, binned by 2° × 2° latitude-longitude. Warmer colors represent higher counts, while cooler colors represent fewer observations. White grid boxes have 10 or fewer cloud clusters across the 11 year period.

different from others [*Lovejoy and Schertzer*, 2006]. Figure 5b shows the kernel density estimate [*Rosenblatt*, 1956; *Parzen*, 1962], a nonparametric estimate of the probability density of maximum areal extent of each cluster across several lifetime bins.

Overall, Figure 5 shows that the frequency of cluster lifetime and size is proportional. This is similar to the results from *Chen and Houze* [1997], who show a linear correlation between the count of tropical cloud clusters with respect to maximum size and lifetime in the western Pacific. This reinforces that shorter-lived events tend to remain small in scale, while longer-lived ones achieve greater horizontal scales.

These results can be compared with event tracking based on model data [e.g., *Bengtsson et al.*, 2006, 2009; *Hoskins and Hodges*, 2002; *Neu et al.*, 2013; *Sinclair*, 1994]. Modeling studies typically use vorticity or sea level pressure as the defining feature of midlatitude cyclone storm tracks. Coupled with lower temporal resolution data, this can result in smoother tracks and are larger and longer lived than the ones shown in Figure 4. The differences are due to tracking definitions but may also be due to the prevalence of lighter rainfall typical in models as compared with observations [*Stephens et al.*, 2010].

4.2. Cloud Cluster Climatology

On the global scale, the clusters exhibit many systematic spatial and temporal characteristics, as seen in the seasonal climatology map of clusters (Figure 6). The map produced is the frequency of clusters at their maximum areal extent for each 2° × 2° latitude-longitude bin. During DJF, the Intertropical Convergence Zone (ITCZ) is closer to the equator and South Pacific convergence zone is intensified. There is increased activity from the midlatitude storm tracks across the North American west coast and Europe. In JJA, tracks capture the northward placement of the ITCZ, Atlantic coastal storms, and the East Asian monsoon. Less activity is
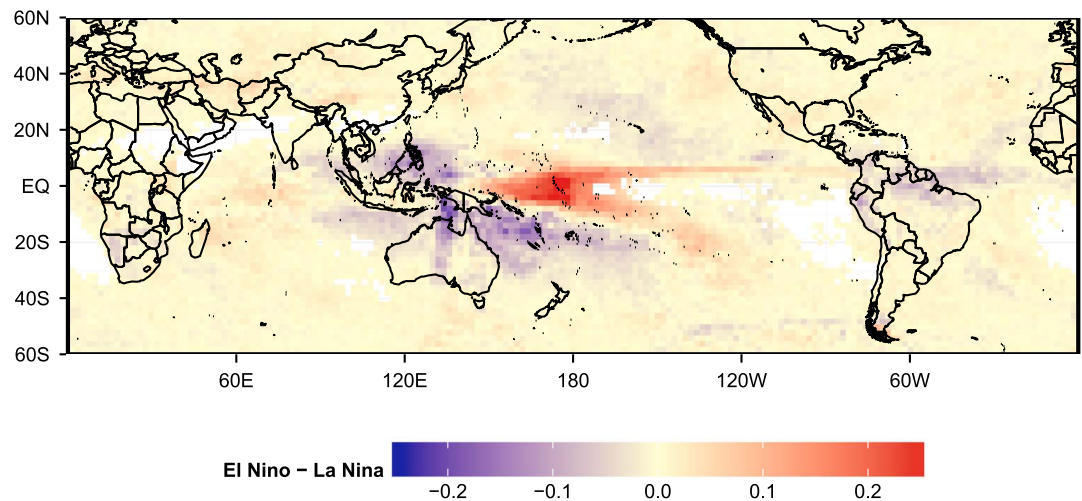
Figure 7. The composite of the 11 year DJF mean annual frequency of cloud cluster overpasses for El Niño and La Niña, binned by 2° × 2° latitude-longitude, at their maximum areal extent. Warm or cool event years were selected based on the NINO3.4 sea surface temperature anomaly index. White grid boxes have three or fewer cloud clusters.

found in proximity of the semipermanent high-pressure systems (e.g., Pacific and Bermuda highs in JJA). Artifacts in South Pacific (40°–60°S, 120°–160°W) are due to calibration differences between geostationary platforms and the interface of the half-hourly and hourly sampling regions of the Geostationary Meteorological Satellite between 120° and 170°E. Note that in Figure 6a, we excluded data from DJF 2006 from 120 to 170°E due to intermittent noisy brightness temperature data in this region.

The frequency also reveals some regional subtleties in Figure 6b. Over the Southeast Asia islands in the western Pacific Ocean, there are roughly twice as many clusters along coastlines than the surrounding oceanic areas. This region's combination of topography, land-sea thermal contrast, and available moisture generates storms that are both large in scale and deep, making it one of the rainiest places on Earth in TRMM-based object studies [*Houze et al.*, 2015].

Interestingly, a high count of clusters does not necessarily correlate with intense rainfall. Outside the ITCZ, the Amazon, the Asian monsoon, and West African monsoon are among the most active continental regions in terms of cluster frequency. However, TRMM-based studies have shown that objects tend to have moderate strength and were larger in scale in the Amazon, while the latter two regions are composed of deep convection [*Zipser et al.*, 2006; *Houze et al.*, 2015]. In the Amazon, rainfall features have a lower mean height than those over the Asian and African monsoon regions and warm rain tends to be the greatest contributor of rainfall [*Liu and Zipser*, 2009]. While not shown, statistically, we found that clusters in our study were typically larger, colder, and longer lived over Western Africa and the Indian subcontinent (JJA), whereas shorter-lived, moderate-sized clusters tended to occur over the Amazon (DJF).

Compared to results based on reanalysis-based tracking results, the JJA cluster counts shown in Figure 6b resemble vorticity-based African Easterly [*Thorncroft and Hodges*, 2001]. In both studies, initiation maxima occur along the West Africa coast and Ethiopian highlands as well as over the Pacific, downstream of Central America. We visually observed that our IR-based tracks are noisier than reanalysis derived ones and are less exclusive. Tracking with 6-hourly data can skew results toward stronger, longer-lived events and can miss younger events.

4.3. Interannual Variability

There is significant interannual variability in cluster occurrence, particularly between El Niño and La Niña years. Figure 7 shows the composite of frequency difference of cluster overpasses at their maximum size during the El Niño phases for 11 years of DJF, binned by 2° × 2° latitude-longitude boxes. This was produced by subtracting the annual average frequency of cluster occurrence during warm phases from the annual average of cool phases. Only seasons with weak, moderate, or strong phases based on the NINO3.4 sea surface temperature anomaly index are included.
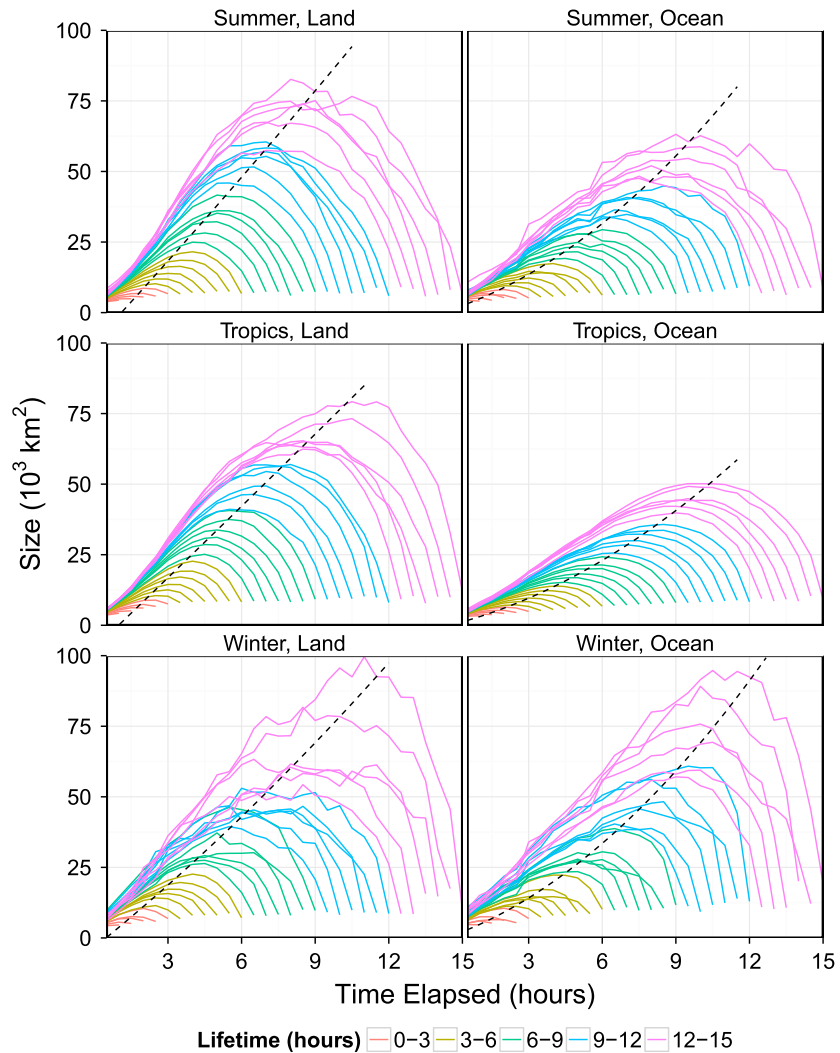
Figure 8. The global average life cycle evolution for new cloud clusters with varying life times. Each curve represents the average properties of millions of clusters grouped by life span. The shortest lines are short-lived events; longer lines are long lived. Curves show how the size changes as a function of the clusters' lifetime. Dashed curve is a regression fitted to the maximum of each curve. Seasons are defined by the $\pm25°$ latitude line.

El Niño has an expected effect on the frequency of cloud clusters in the tropics: more clusters are observed near the equator during the warm phase in the central Pacific (160°E–160°W) and in the western Pacific (110°–160°E) during the cool phase. However, teleconnections can also be observed; there is an increase in occurrence over the Northwest United States (25°–55°N, 100–120°W) and Indian Ocean (10°S–10°N, 40°–80° E) and a decrease in the Atlantic basin (10°S–10°N, 60°–10°W) during El Niño. *Teng et al.* [2014] have shown that there are both increases in cloud cluster occurrence as well as their likelihood of forming tropical cyclones in the western North Pacific during El Niño.

4.4. Life Cycle of Cloud Clusters

The advantage of continuous Lagrangian tracking is that it allows us to examine systematically the clusters' full life cycle and the associated evolution of their characteristics. Figures 8 and 9 show how the size and brightness temperature of clusters evolve throughout their lifespan. Each curve represents the average of the aggregated clusters that lived to the same age. For clarity, clusters that merged into or split off from existing clusters were not included in Figures 8 and 9. Shorter curves represent brief events, while longer lines represent clusters with longer lifespans. The observed mean life cycles have well-defined stages of
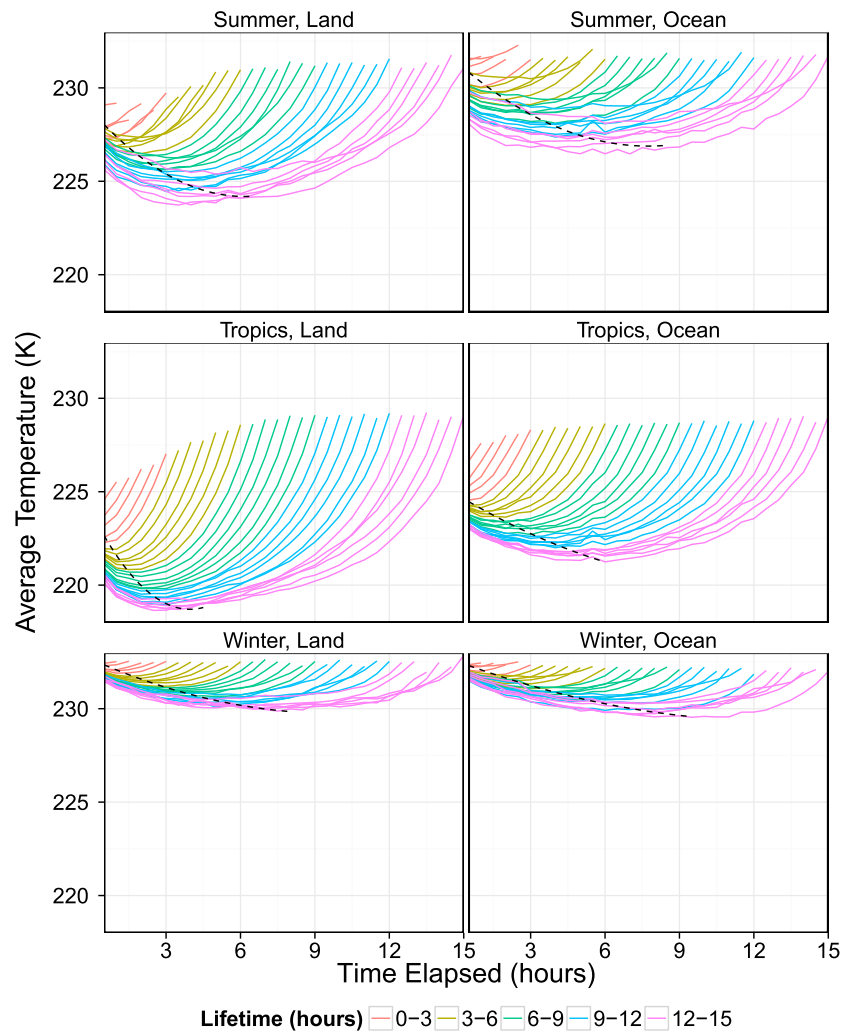
Figure 9. Same as Figure 8 but showing how the average brightness temperature changes as a function of time and lifetime.

development—initial detection, intensification, maturity, and decay. This can be seen in both their size evolution (Figure 8) and brightness temperature evolution (Figure 9). With respect to size, clusters initiate, grow, and achieve their areal maximum closer to the end of their life cycle (Figure 8). At their size maximum, longer-lived clusters can double or triple their initial areal extent. Shorter-lived ones undergo rapid decay early in their cycle. In contrast, during their brightness temperature life cycle, clusters cool to a minimum and then begin to warm for the rest of the life cycle (Figure 9). While an individual clusters' evolution usually appears erratic and unpredictable, collectively, their mean behavior computed from the ensemble of 10 million clusters shows regularity.

The minimum brightness temperature is reached at an earlier point in the clusters life cycle than the size maximum. This could be due to overshooting tops, which reach deep into the troposphere or lower stratosphere first and then expand to form anvils as they cool, and thus attaining their minimum brightness temperature before their maximum areal extent. Additionally, clusters at their maximum areal extent produce cirrus shields that can also conceal the true extent of the clusters underneath.

On the global scale, the life cycle evolution shows substantial differences over contrasting seasons and land surfaces. Due to their similarity, in Figures 8 and 9 regions are divided into seasons along the ±25° latitude line, where northern and southern winters (summers) are during DJF and JJA (JJA and DJF), respectively. The tropics use data from both seasons. Generally, growth is more vigorous in summer than in winter (e.g.,
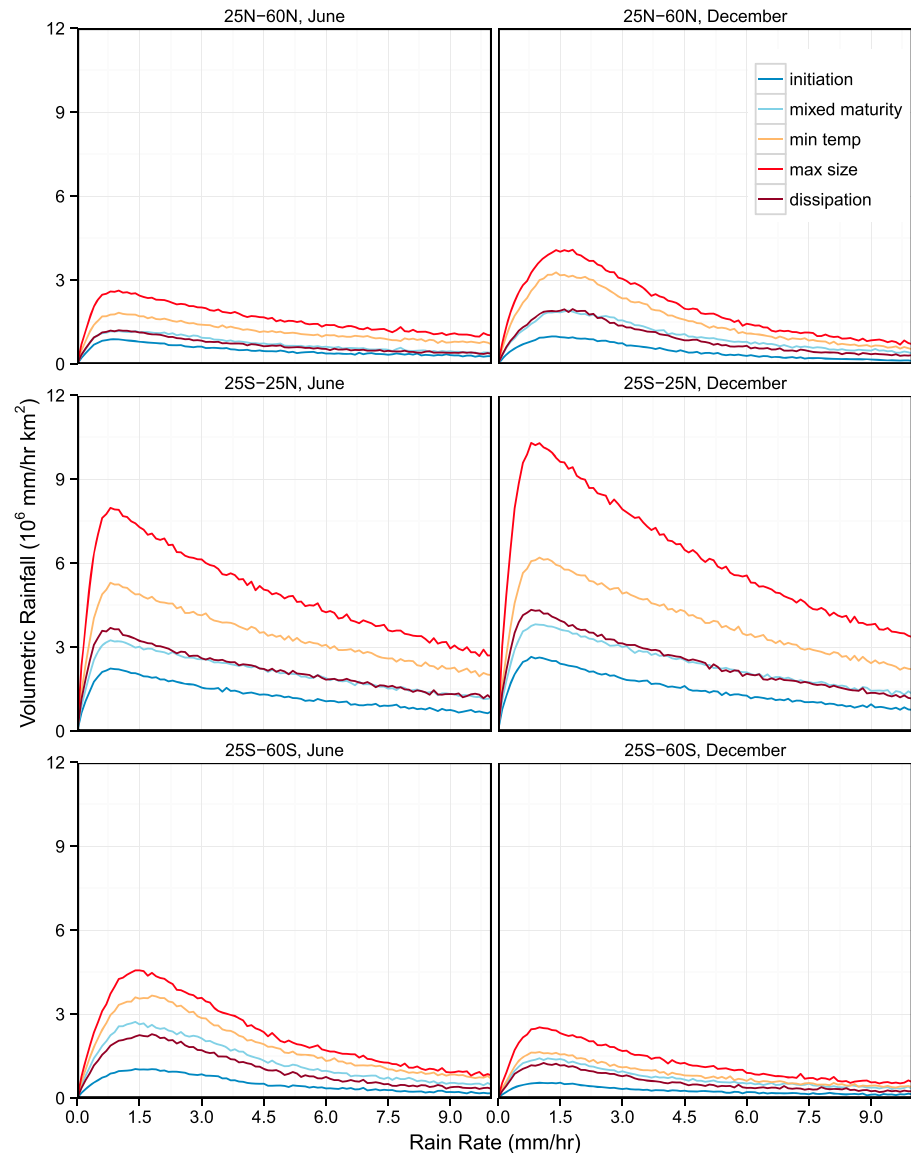
Figure 10. Total instantaneous rainfall contribution as a function of rain rate captured by clusters in the (a, b) Northern Hemisphere, (c, d) tropics, and (e, f) Southern Hemisphere in June and December 2014. The distribution is based on coincident cloud clusters and passive microwave-based rainfall estimates from the IMERG data set.

compare Figures 8b and 8f to Figures 9b and 9f), over land than over ocean (e.g., compare Figures 8a and 8b to Figures 9a and 9b). In addition, the wintertime clusters are much larger than summertime (e.g., Figures 8a and 8e). In the summer, the midlatitude size curves (Figures 8a and 8b) are more similar to the tropics (Figures 8c and 8d). Regarding brightness temperature, there is a larger spread during the summer (Figures 9a and 9b) and in tropics (Figures 9c and 9d) than during the winter for both land and ocean (Figures 9e and 9f). Clusters in the tropics (Figures 9c and 9d) are significantly cooler than higher latitudes due to deep convection (Figures 9a and 9b).

The peaks in Figures 8 and 9 were fitted to a quadratic linear regression model to show the general trend of size and temperature maturity across different lifetimes. Shorter-lived clusters tended to be already at maturity at the time of detection—that is, the shortest lines in Figures 8 and 9 show that these clusters' total area decreased and temperatures rapidly increased. For longer-lived clusters, the timing of the maximum areal extent and minimum temperature was asynchronous and larger than that for shorter-lived events. We will examine some of the implications of this in the following sections.
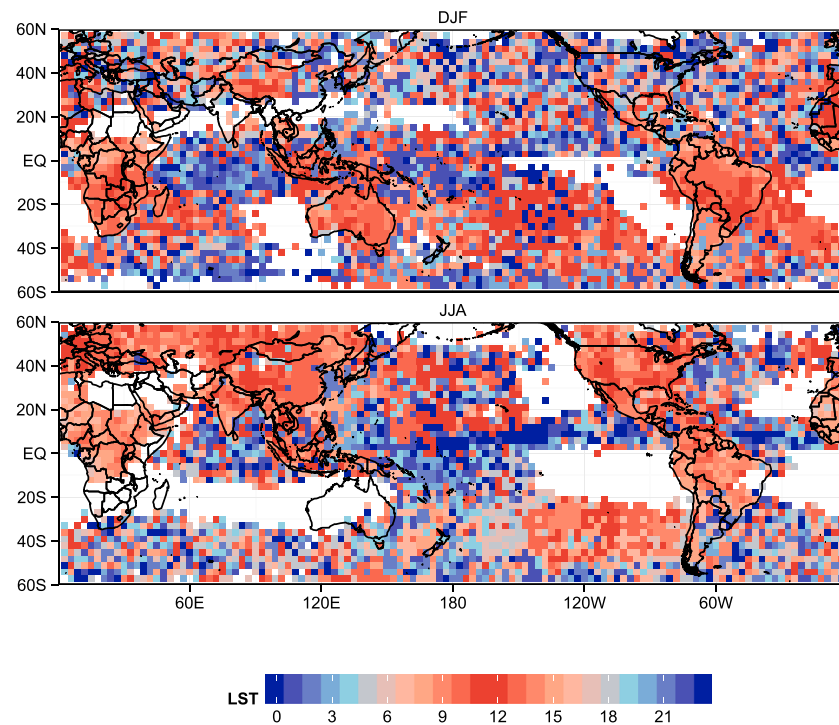
Figure 11. Diurnal variation in local solar time (LST) cloud cluster initiation for (top) DJF and (bottom) JJA, binned by 2° × 2° latitude-longitude. Each box shows the timing of maximum occurrence of cluster formation for the 11 year record. Only clusters with a lifetime greater than 2 h are included.

4.5. Cloud Clusters and Rainfall

In raining cloud clusters, the differences in the timing of the minimum brightness temperature and maximum size contribute varying amounts to total precipitation. In Figure 10, we identified several distinct life cycle stages (initiation, mixed maturity, minimum brightness temperature, maximum size, and dissipation) and the instantaneous total volumetric rainfall that is attributed to each rain rate bin. Using the procedure detailed in section 3.3, this was determined by collocating the cloud clusters with available microwave-only rainfall estimations from IMERG [*Huffman et al.*, 2013], for June and December 2014.

Due to the lower temporal resolution of polar-orbiting satellites, most clouds could only be sampled once, so results are examined in a statistical sense rather than as totals by individual objects. Here we define the minimum temperature (maximum size) as the lowest average temperature (largest areal extent) achieved by clusters. This is similar to the definition used by *Futyan and Del Genio* [2007]. We also divide contribution into two mutually exclusive maturity states, synchronous and asynchronous occurrence of minimum temperature and maximum areal extent. The prior is denoted as mixed maturity, while the latter is broken down into the two stages of its variables. Collectively, the figure shows the rainfall contribution of the beginning, mature, and final life cycle stage.

Initially, raining clusters are composed of lighter rain and produce less of it. As development continues, they produce larger volumes of rain as the areal extent of the cloud increases. It is interesting that in all cases, mixed maturity clusters contribute less rainfall than those with asynchronous stages. These cases tended to be shorter lived on average (1.9 h) than those with larger differences in timing (2.9 h).

There are seasonal differences in these values. The winter midlatitudes (Figures 10b and 10e) produced more overall rain than their corresponding summer hemisphere (Figures 10a and 10f) and were more heavily skewed toward lighter rainfall. The tropics had less seasonal variation in rainfall contribution (Figures 10c and 10d).

Precipitation retrieval algorithms may benefit from incorporating information on the life cycle stage, season, and hemisphere of the IR cloud cluster. In morphing techniques, the shape and intensity of rain clusters is
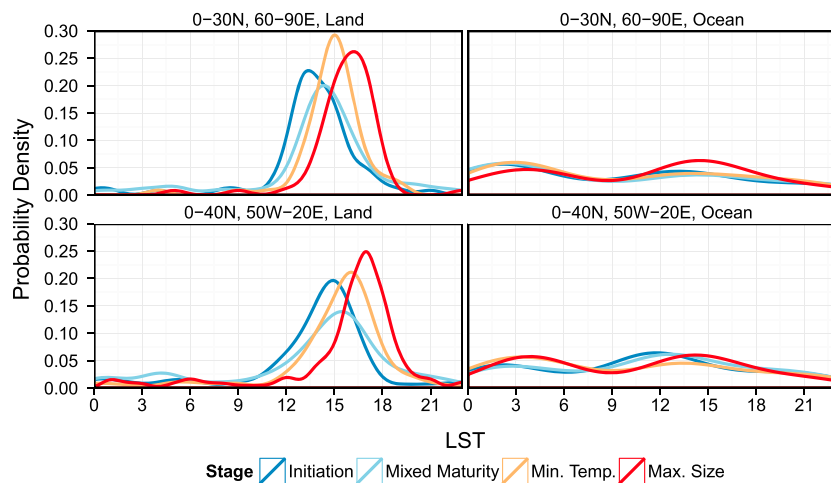
Figure 12. The kernel density of local solar time of the life cycle stage in two regions, 0°–30°N and 60°–90°E (South Asia) and 0°–40°N, 50°W–20°E (West Africa).

held constant between overpasses [*Joyce et al.*, 2004], while in Figures 8 and 9 we show that both horizontal size and temperature growth rates are not constant during cloud cluster evolution. Biases in hourly rain volume estimates vary across life cycle stages, lifetimes, and precipitation algorithm [*Tadesse and Anagnostou*, 2009]. Knowing the age of the cloud could be useful in devising the next-generation multisensor algorithms.

4.6. Diurnal Cycle of Cluster Evolution

By continuously tracking cloud clusters, we can study when and where they reach their life cycle milestones. Figure 11 shows the local solar time (LST) of the maximum in the frequency of cluster initiation. This was calculated from frequency maximum at each hourly, $2° \times 2°$ bin for clusters with a lifetime greater than 2 h. Over land, peak cloud initiation occurs in the afternoon, especially in the summer hemisphere. Over the ocean, there is greater prevalence of early morning and afternoon clouds, but the timing of peak activity depends on region. This double peak was also previously found in the West Pacific warm pool by *Chen and Houze* [1997]. To examine these differences in context of development stage, we examine two regions centered over West Africa (0°–40°N, 50°W–20°E) and the South Asian peninsula (0°–30°N and 60°–90°E).

In Figure 12, we examine the kernel density of the LST by cluster life cycle stage in these two regions for both seasons. Over land, there is a strong diurnal cycle and a lag in the local timing of initiation, minimum temperature, and maximum size. The timing differences are much smaller over the ocean in both regions, and there is a semidiurnal cycle over the ocean. This is consistent with *Futyan and Del Genio* [2007] for equatorial Africa and the Atlantic Ocean. The timing of peak initiation over land is earlier in the South Asian region (1300 LST) than in the Western Africa region (1500 LST). This is possibly due to the windward side of the Indian subcontinent skewing the population to lower initiation times. Over the ocean, the early morning peaks have similar timing (0200 LST), but the afternoon peak in Western Africa is earlier (1100 versus 1300 LST). *Kikuchi and Wang* [2008] observed this semidiurnal cycle over the Pacific, Indian, and Atlantic Oceans in empirical orthogonal modes of TRMM data sets. We can take advantage of the known lifetime and further inspect the duration of these cloud clusters at different times of the day.

In Figure 13, we show the kernel density for the LST grouped by the 3-hourly binned lifetime. Over land, the timing differences were delayed by not more than an hour for all lifetime groups. Shorter-lived clusters (those with lifetimes 6 h or less) had a sharper peak than longer-lived events (those with lifetimes greater than 6 h). There are trivial differences in the onset of short- versus long-lived events in the South Asia region than over West Africa.

However, over the ocean, longer-lived clusters had a greater tendency to occur in the early morning hours, peaking between 0300–0400 and 0400–0500 LST in South Asia and West Africa, respectively. Shorter-lived events peaked both in the early morning and afternoon but were the primary type in the afternoon between
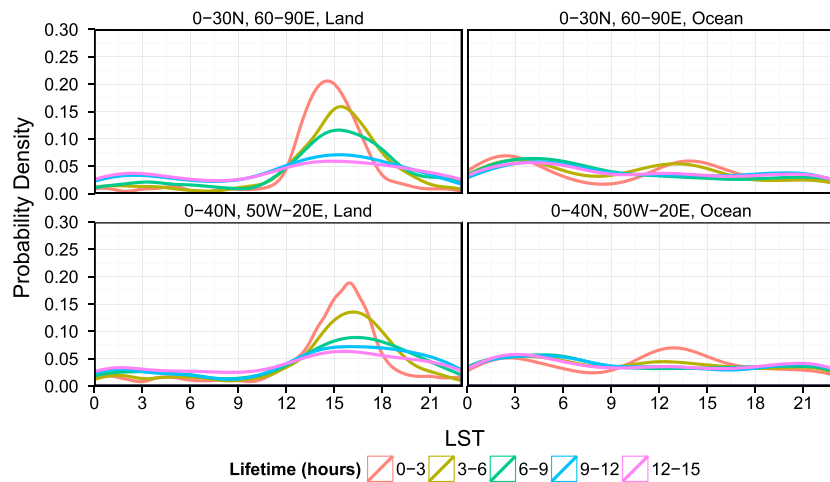
Figure 13. The kernel density of local solar time of initiation in 3-hourly lifetime bins for two regions, 0°–30°N and 60°–90°E (South Asia) and 0°–40°N, 50°W–20°E (West Africa).

1200 and 1300 LST for both regions. In South Asia, the maxima of short-lived clusters precede that of long-lived ones by an hour, partly due to rapid growth and decay of isolated convective cells which upon visual inspection are more numerous in this region than in West Africa. These results are interesting in light of previous examination of TRMM precipitation features, which show that nocturnal storms are more intense over the ocean while over land the strongest storms are observed during the day [*Zipser et al.*, 2006]. In summary, the oceanic semidiurnal cycle can be understood to be composed of not just two different size classes but as cloud clusters with differing lifetimes as well.

Expanding on the study by *Chen and Houze* [1997], our results show that their results extend beyond the West Pacific to other regions and over longer time periods. Chen and Houze found that large-scale, long-lived clusters follow a 2 day cycle. The formation of long-lived clusters suppresses subsequent development in that area due to dry downdrafts from strong storms and the reduction in sea surface temperatures due to cloud canopy shading. Examining the development-suppression cycle of cloud clusters in other oceanic regions could be an interesting future direction for this work.

5. Summary and Discussion

In this study, we tracked cloud clusters on the global scale to study the climatology and life cycles across a broad class of clusters using 11 years of the high-resolution, satellite-based globally merged cloud brightness temperature data. We examined the trajectories, climatology, life cycles, and diurnal cycle of clusters in context of their life cycle stage and lifetime.

We found that the vast majority of clusters are short lived and small, demonstrating the need to work with high-resolution data to fill in coverage gaps. Differences in the shapes and scales of life cycle curves reflect the variety of clouds captured and show that evolution is a complex process. Development over the oceans is less intense compared to land, where strong thermal contrast, orography, and aerosols can influence evolution. We observe a larger lag in the occurrence of minimum temperature and maximum size for longer-lived cloud clusters, particularly over land. The diurnal cycle of cloud clusters over the South Asia and West Africa revealed a strong diurnal peak over land and a semidiurnal cycle over the ocean, the latter of which showed greater prevalence of shorter-lived cloud clusters in the afternoon and dominance of longer-lived events in the early morning.

The capability for infrared data to reliably identify and track smaller-scale convective systems is an aspect in which global climate models still have difficulties [*Stephens et al.*, 2010; *Westra et al.*, 2014]. Thus, IR-based cloud tracking can be used to evaluate the effectiveness of the downscaling abilities of models [*Boer and Ramanathan*, 1997]. On the other hand, the infrared data can only depict the two-dimensional, cloud top

characteristics of the clusters. To address the complex three-dimensional hydrothermodynamics of cloud systems, one has to combine observations from other satellites, such as CloudSat and CALIPSO, with reanalysis data.

There are several limitations to this study that represent an area of ongoing work, particularly regarding thresholds. Being too selective on size scales can exclude these events; being too relaxed produces too many splits, which prematurely terminates the cluster. Cold surfaces are a particular challenge, such as the Tibetan Plateau which is dry in the northern winter. However, the relatively high frequency over this region in Figure 6 a indicates that mountain glacier surfaces are incorrectly being captured in this region. This poses a challenge to other tracking studies, and mountainous areas are sometimes removed from analysis [*Neu et al.*, 2013]. As a future improvement, we could develop a dynamic threshold criteria rather than a fixed brightness temperature value [*Hennon et al.*, 2011].

Another challenge lies in the early termination of cloud clusters due to splits and mergers. As clouds evolve, they continuously split and merge, each of which resets the lifetime clock to zero. Only the largest, most well defined clusters avoid this in their lifetimes. This is a limitation of this specific technique, but the tracking algorithm could be refined in the future to track features that do not have an easily defined shape, such as wintertime midlatitude storms or the movement of clouds that are part of atmospheric rivers.

In spite of such limitations, there are many promising areas of future work. The cluster tracking provided in this study can be combined with other event-based data sets, such as the TRMM precipitation feature (TRMM-PF) data set developed by *Liu et al.* [2008]. TRMM-PF has been extensively used to study the scale and intensity of rainfall events and can infer life cycle stage from the vertical profiles obtained from the precipitation radar. By combing TRMM-PF with our IR-based cloud tracks, rain features can be studied in context of their entire life cycle and trajectory, overcoming the sampling limits of polar-orbiting satellites, to further our understanding of precipitating cloud systems.

References

Bengtsson, L., K. I. Hodges, and E. Roeckner (2006), Storm tracks and climate change, *J. Clim.*, *19*(15), 3518–3543.

Bengtsson, L., K. I. Hodges, and N. Keenlyside (2009), Will extratropical storms intensify in a warmer climate?, *J. Clim.*, *22*(9), 2276–2301, doi:10.1175/2008JCLI2678.1.

Blamey, R. C., and C. J. C. Reason (2012), Mesoscale convective complexes over Southern Africa, *J. Clim.*, *25*(2), 753–766, doi:10.1175/JCLI-D-10-05013.1.

Boer, E. R., and V. Ramanathan (1997), Lagrangian approach for deriving cloud characteristics from satellite observations and its implications to cloud parameterization, *J. Geophys. Res.*, *102*(D17), 21,383–21,399, doi:10.1029/97JD00930.

Carvalho, L. M. V., and C. Jones (2001), A satellite method to identify structural properties of mesoscale convective systems based on the maximum spatial correlation tracking technique (MASCOTTE), *J. Appl. Meteorol.*, *40*(10), 1683–1701, doi:10.1175/1520-0450.

Chen, S. S., and R. A. Houze (1997), Diurnal variation and life-cycle of deep convective systems over the tropical Pacific warm pool, *Q. J. R. Meteorol. Soc.*, *123*(538), 357–388, doi:10.1002/qj.49712353806.

Chen, S. S., R. A. Houze Jr., and B. E. Mapes (1996), Multiscale variability of deep convection in relation to large-scale circulation in TOGA COARE, *J. Atmos. Sci.*, *53*(10), 1380.

Ebert, E. E., J. E. Janowiak, and C. Kidd (2007), Comparison of near-real-time precipitation estimates from satellite observations and numerical models, *Bull. Am. Meteorol. Soc.*, *88*(1), 47–64, doi:10.1175/BAMS-88-1-47.

Fiolleau, T., and R. Roca (2013), An algorithm for the detection and tracking of tropical mesoscale convective systems using infrared images from geostationary satellite, *IEEE Trans. Geosci. Remote*, *51*(7), 4302–4315, doi:10.1109/TGRS.2012.2227762.

Futyan, J. M., and A. D. Del Genio (2007), Deep convective system evolution over Africa and the tropical Atlantic, *J. Clim.*, *20*(20), 5041–5060, doi:10.1175/JCLI4297.1.

Hennon, C. C., C. N. Helms, K. R. Knapp, and A. R. Bowen (2011), An objective algorithm for detecting and tracking tropical cloud clusters: Implications for tropical cyclogenesis prediction, *J. Atmos. Oceanic Technol.*, *28*(8), 1007–1018, doi:10.1175/2010JTECHA1522.1.

Hoskins, B. J., and K. I. Hodges (2002), New perspectives on the Northern Hemisphere winter storm tracks, *Atmos. Sci.*, *59*(6), 1041–1061.

Hou, A. Y., R. K. Kakar, S. Neeck, A. A. Azarbarzin, C. D. Kummerow, M. Kojima, R. Oki, K. Nakamura, and T. Iguchi (2013), The global precipitation measurement mission, *Bull. Am. Meteorol. Soc.*, *95*(5), 701–722, doi:10.1175/BAMS-D-13-00164.1.

Houze, R. A., Jr., K. L. Rasmussen, M. D. Zuluaga, and S. R. Brodzik (2015), The variable nature of convection in the tropics and subtropics: A legacy of 16 years of the Tropical Rainfall Measuring Mission (TRMM) satellite, *Rev. Geophys.*, *53*, 994–1021, doi:10.1002/2015RG000488.

Huffman, G. J., D. T. Bolvin, E. J. Nelkin, D. B. Wolff, R. F. Adler, G. Gu, Y. Hong, K. P. Bowman, and E. F. Stocker (2007), The TRMM Multisatellite Precipitation Analysis (TMPA): Quasi-global, multiyear, combined-sensor precipitation estimates at fine scales, *J. Hydrometeorol.*, *8*(1), 38–55.

Huffman, G. J., D. Bolvin, D. Braithwaite, K. Hsu, R. Joyce, and P. Xie (2013), NASA Global Precipitation Measurement (GPM) Integrated Multi-satellitE Retrievals for GPM (IMERG). Algorithm Theoretical Basis Doc., version 4.1, NASA, 29 pp. [Available at http://pmm.nasa.gov/sites/default/files/document_files/IMERG_ATBD_V4.1.pdf.]

Janowiak, J. E., R. J. Joyce, and Y. Yarosh (2001), A real-time global half-hourly pixel-resolution infrared dataset and its applications, *Bull. Am. Meteorol. Soc.*, *82*(2), 205–217, doi:10.1175/1520-0477.

Joyce, R. J., J. E. Janowiak, P. A. Arkin, and P. Xie (2004), CMORPH: A method that produces global precipitation estimates from passive microwave and infrared data at high spatial and temporal resolution, *J. Hydrometeorol.*, *5*(3), 487–503.

Kikuchi, K., and B. Wang (2008), Diurnal precipitation regimes in the global tropics*, *J. Clim.*, *21*(11), 2680–2696, doi:10.1175/2007JCLI2051.1.

Kubota, T., and S. Shige (2007), Global precipitation map using satellite-borne microwave radiometers by the GSMaP Project: Production and validation, *IEEE Trans. Geosci. Remote Sens.*, *45*(7), 2259–2275, doi:10.1109/TGRS.2007.895337.

Kummerow, C., et al. (2000), The status of the Tropical Rainfall Measuring Mission (TRMM) after two years in orbit, *J. Appl. Meteorol.*, *39*(12), 1965–1982, doi:10.1175/1520-0450(2001)040<1965:TSOTTR>2.0.CO;2.

Laing, A. G., and J. M. Fritsch (1997), The global population of mesoscale convective complexes, *Q. J. R. Meteorol. Soc.*, *123*(538), 389–405, doi:10.1002/qj.49712353807.

Lakshmanan, V., K. Hondl, and R. Rabin (2009), An efficient, general-purpose technique for identifying storm cells in geospatial images, *J. Atmos. Oceanic Technol.*, *26*(3), 523–537, doi:10.1175/2008JTECHA1153.1.

Li, J., K. Hsu, A. AghaKouchak, and S. Sorooshian (2015), An object-based approach for verification of precipitation estimation, *Int. J. Remote Sens.*, *36*(2), 513–529, doi:10.1080/01431161.2014.999170.

Liu, C., and E. J. Zipser (2009), "Warm Rain" in the tropics: Seasonal and regional distributions based on 9 yr of TRMM data, *J. Clim.*, *22*(3), 767–779, doi:10.1175/2008JCLI2641.1.

Liu, C., E. J. Zipser, D. J. Cecil, S. W. Nesbitt, and S. Sherwood (2008), A cloud and precipitation feature database from nine years of TRMM observations, *J. Appl. Meteorol. Climatol.*, *47*(10), 2712–2728, doi:10.1175/2008JAMC1890.1.

Lovejoy, S., and D. Schertzer (2006), Multifractals, cloud radiances and rain, *J. Hydrol.*, *322*(1-4), 59–88, doi:10.1016/j.jhydro1.2005.02.042.

Machado, L. A. T., and H. Laurent (2004), The convective system area expansion over Amazonia and its relationships with convective system life duration and high-level wind divergence, *Mon. Weather Rev.*, *132*(3), 714–725.

Machado, L. A. T., M. Desbois, and J.-P. Duvel (1992), Structural characteristics of deep convective systems over tropical Africa and the Atlantic Ocean, *Mon. Weather Rev.*, *120*(3), 392–406, doi:10.1175/1520-0493(1992)120<0392:SCODCS>2.0.CO;2.

Machado, L. A. T., W. B. Rossow, R. L. Guedes, and A. W. Walker (1998), Life cycle variations of mesoscale convective systems over the Americas, *Mon. Weather Rev.*, *126*(6), 1630–1654.

Maddox, R. A. (1980), Meoscale convective complexes, *Bull. Am. Meteorol. Soc.*, *61*(11), 1374–1387, doi:10.1175/1520-0477.

Mapes, B. E., and R. A. Houze (1993), Cloud clusters and superclusters over the oceanic warm pool, *Mon. Weather Rev.*, *121*(5), 1398–1416, doi:10.1175/1520-0493.

Morel, C., and S. Senesi (2002), A climatology of mesoscale convective systems over Europe using satellite infrared imagery. II: Characteristics of European mesoscale convective systems, *Q. J. R. Meteorol. Soc.*, *128*(584), 1973–1995, doi:10.1256/003590002320603494.

Neu, U., et al. (2013), IMILAST: A community effort to intercompare extratropical cyclone detection and tracking algorithms, *Bull. Am. Meteorol. Soc.*, *94*(4), 529–547, doi:10.1175/BAMS-D-11-00154.1.

Parzen, E. (1962), On estimation of a probability density function and mode, *Ann. Math. Stat.*, *33*(3), 1065–1076, doi:10.1214/aoms/1177704472.

Rosenblatt, M. (1956), Remarks on some nonparametric estimates of a density function, *Ann. Math. Stat.*, *27*(3), 832–837, doi:10.1214/aoms/1177728190.

Sinclair, M. R. (1994), An objective cyclone climatology for the Southern Hemisphere, *Mon. Weather Rev.*, *122*(10), 2239–2256, doi:10.1175/1520-0493.

Stephens, G. L., T. L'Ecuyer, R. Forbes, A. Gettlemen, J.-C. Golaz, A. Bodas-Salcedo, K. Suzuki, P. Gabriel, and J. Haynes (2010), Dreary state of precipitation in global models, *J. Geophys. Res.*, *115*, D24211, doi:10.1029/2010JD014532.

Tadesse, A., and E. N. Anagnostou (2009), The effect of storm life cycle on satellite rainfall estimation error, *J. Atmos. Oceanic Technol.*, *26*(4), 769–777, doi:10.1175/2008JTECHA1129.1.

Teng, H.-F., C.-S. Lee, and H.-H. Hsu (2014), Influence of ENSO on formation of tropical cloud clusters and their development into tropical cyclones in the western North Pacific: Influence of ENSO on TCC Formation, *Geophys. Res. Lett.*, *41*, 9120–9126, doi:10.1002/2014GL061823.

Thorncroft, C., and K. Hodges (2001), African easterly wave variability and its relationship to Atlantic tropical cyclone activity, *J. Clim.*, *14*(6), 1166–1179, doi:10.1175/1520-0442(2001)014<1166:AEWVAI>2.0.CO;2.

Velasco, I., and J. Fritsch (1987), Mesoscale convective complexes in the Americas, *J. Geophys. Res.*, *92*(D8), 9591–9613, doi:10.1029/JD092iD08p09591.

Vila, D. A., L. A. T. Machado, H. Laurent, and I. Velasco (2008), Forecast and Tracking the Evolution of Cloud Clusters (ForTraCC) using satellite infrared imagery: Methodology and validation, *Weather Forecasting*, *23*(2), 233–245.

Westra, S., H. J. Fowler, J. P. Evans, L. V. Alexander, P. Berg, F. Johnson, E. J. Kendon, G. Lenderink, and N. M. Roberts (2014), Future changes to the intensity and frequency of short-duration extreme rainfall, *Rev. Geophys.*, *52*, 522–555, doi:10.1002/2014RG000464.

Williams, M., and R. A. Houze (1987), Satellite-observed characteristics of winter monsoon cloud clusters, *Mon. Weather Rev.*, *115*(2), 505–519, doi:10.1175/1520-0493.

Xie, P., and A.-Y. Xiong (2011), A conceptual model for constructing high-resolution gauge-satellite merged precipitation analyses, *J. Geophys. Res.*, *116*, D21106, doi:10.1029/2011JD016118.

Zipser, E. J., D. J. Cecil, C. Liu, S. W. Nesbitt, and D. P. Yorty (2006), Where are the most intense thunderstorms on Earth?, *Bull. Am. Meteorol. Soc.*, *87*(8), 1057, doi:10.1175/BAMS-87-8-1057.

Erratum

In the originally published version of this article, parts (a) and (b) of Figure 1 were mislabeled. This has since been corrected and this version may be considered the authoritative version of record.